# Preliminary Results of Angle-Resolved BTDF Characterization of Optical Transmissive Diffusers

Jinglin Fu[1], Jeppe R. Frisvad[2], Michael Esslinger[1], Tatjana Quast[1] and Alfred Schirmacher[1]

[1] *Physikalisch-Technische Bundesanstalt, Bundesallee 100, 38116 Braunschweig, Germany*
[2] *Department of Applied Mathematics and Computer Science, Technical University of Denmark, Richard Petersens Plads, Building 324, 2800 Kgs. Lyngby, Denmark*

**Abstract**

Optical diffusers are used in many application areas related to illumination. With the purpose of characterizing the transmission properties of optical diffusers, we present preliminary results of BTDF (Bidirectional Transmittance Distribution Function) measurement with high angular resolution at two different wavelengths. The expanded total uncertainty of the measurement is estimated to be 0.5% in the best case. In this way, the scattering distribution of optical diffusers could be quantitatively described by their BTDF values with high precision, good repeatability and reproducibility. The diffusers' angle-dependent spectral transmittances in the VIS (from 380 nm to 780 nm in the electromagnetic spectrum) are also measured using a commercially available spectrophotometer. Results are compared to simulation calculated from a simple model and a first-step explanation for the sample spectral dependency is proposed.

**Keywords**

Optical Diffuser, Diffuse Transmission, BTDF, Angle-resolved Detection, Wavelength Dependency



## 1. Introduction

When light impinges on a rough surface or propagates through a thin layer with non-uniformities in the material, it will deviate from its original trajectory and be scattered. Depending on the type of interaction, in its extremes the reflection and transmission of light are distinguished and described as either specular or diffuse. In most cases however, the situation is a mixture of these two components. Optical diffuse transmission happens almost everywhere in our daily life and people have been constantly making great use of it. In the field of satellite-based Earth remote sensing, for example, optical transmissive diffusers are used for the calibration of the on-orbit spectral radiance [1, 2]. In illumination design, diffusers are integrated in the optical system to control the distribution of transmitted light [3, 4]. In computer graphics rendering, "diffusers" are also used in different scenarios to simulate the transfer of light through thin objects in a realistic way [5, 6, 7, 8].

Characterization of diffuse transmission is of great importance, because it provides important information on the visual appearance of an object. A quantitative characterization of optical diffusers would be beneficial to both industrial and metrological aspects. Within the JRP EMPIR project *BxDiff* (New quantities for the measurement of appearance) [9], different types of measurands (BRDF, BTDF, BSSRDF) are determined to lay a foundation for better understanding the characterization of the visual appearance of objects. In this paper, preliminary results of the angle-resolved measurement on the BTDF of five different types of diffusers are presented. Measurements were carried out at PTB (Physikalisch-Technische Bundesanstalt), the national metrology institute in Germany. The combined

*The 11th Colour and Visual Computing Symposium 2022, September 08–09, 2022, Gjøvik, Norway*
EMAIL: jinglin.fu@ptb.de (A. 1); jerf@dtu.dk (A. 2); michael.esslinger@ptb.de (A. 3); tatjana.quast@ptb.de (A. 4); alfred.schirmacher@ptb.de (A. 5)
ORCID: 0000-0001-8260-8017 (A. 1); 0000-0002-0603-3669 (A. 2); 0000-0002-2228-7853 (A. 5)

total uncertainty depends on the scattering angle as well as the characteristics of the sample and is estimated to be around 0.5% in the best case. The spectral transmittance at different scattering angles is also measured on another setup and compared to the first-step simulation result. A possible explanation for the wavelength behavior is also proposed in the paper.

# 2. Method

## 2.1. Bidirectional Transmittance Distribution Function (BTDF)

To fully characterize diffusely scattered light, the BRDF (Bidirectional Reflectance Distribution Function) was first introduced by Nicodemus [10, 11]. Bartell et al. [12] then extended this concept into the field of transmission by introducing an analogous term called BTDF (Bidirectional Transmittance Distribution Function). As illustrated in Figure 1(a), a thin sample with flat surface element $\mathrm{d}A_i$ possesses uniform and isotropic scattering properties. Its top surface is uniformly irradiated by a differential element of irradiance $\mathrm{d}E_i$ from a spatial direction described by $(\theta_i, \phi_i)$. The BTDF is then defined as the ratio of the scattered transmitted radiance $\mathrm{d}L_t$ in another specific direction $(\theta_t, \phi_t)$, which is in the transmittance hemisphere of the sample, to the incident irradiance within $\mathrm{d}A_i$:

$$\mathrm{BTDF}(\theta_i, \phi_i; \theta_t, \phi_t) = \frac{\mathrm{d}L_t(\theta_t, \phi_t)}{\mathrm{d}E_i(\theta_i, \phi_i)}, \tag{1}$$

where $\theta$ is the polar angle with respect to the normal of the top surface of the sample (positive direction of the z-axis in Figure 1) and $\phi$ is the azimuth angle within the sample surface plane. The subscripts "i" and "t" designate incident and transmitted radiation, respectively.

By using a differential expression, the BTDF purely describes sample properties as a geometric distribution. It characterizes the transmitting properties of one point on the sample in one specific direction, with contributions from the entire incident radiant flux confined within a certain solid angle. It takes positive values with the unit per steradian ($\mathrm{sr}^{-1}$) [11]. Besides its geometrical sense, the BTDF is also related to parameters such as wavelength and polarization of the incident radiation. Thus, the BTDF is typically expressed as unpolarized values at a certain wavelength.

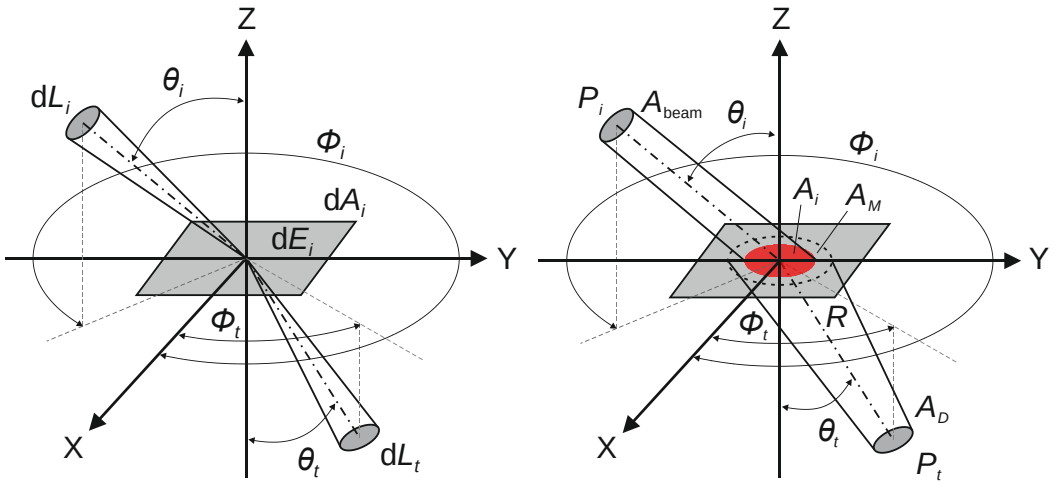


(a) (b)

**Figure 1**: Geometry of BTDF: (a) general definition and (b) measurement

In practice, however, measurements cannot be realized with infinitesimal quantities. Stover [13] suggested the measurement conditions to be modified so that measurements are performed with finite resolution, which is defined by the aperture size of the detection system. It is usually larger than the irradiation spot of the incident beam and large enough for a sufficiently good signal-to-noise level, but in the meantime as small as possible to minimize the influence from the instrument itself on the measured values, which is the convolution of the real BTDF of the sample and the instrument signature. Since a real sample cannot be perfectly isotropic and uniform, measurements of BTDF should be

considered as an average over a surface area which is much larger than the size of the statistical features of the sample [12]. As depicted in Figure 1(b), a sample is irradiated by a collimated beam with finite beam size $A_{\mathrm{beam}}$ and its projection on the sample surface is then

$$A_i = A_{\mathrm{beam}} / \cos\theta_i. \tag{2}$$

The average incident irradiance $E_i$ within $A_i$ on the sample surface takes

$$E_i = \frac{P_i}{A_i}, \tag{3}$$

with $P_i$ the incident optical power measured when no sample is placed in the beam path. The average transmitted radiance $L_t$ is the scattered optical power $P_t$ detected on the other side of the sample within $A_i$ through the detector solid angle $\Omega_t$:

$$L_t = \frac{P_t}{A_i} \cdot \frac{1}{\Omega_t \cos\theta_t}, \tag{4}$$

where $\Omega_t$ is determined by the detector aperture size $A_D$ and the distance $R$ between the detector aperture and the sample back surface (front surface is the irradiated side):

$$\Omega_t = \frac{A_D}{R^2}, \tag{5}$$

and the product of $\Omega_t$ and $\cos\theta_t$ is the projected solid angle at scattering angle $\theta_t$. Combining equations (2) to (5), we obtain the form for evaluating the BTDF from measured signals, when $A_i$ is relatively small and the detector's field of view is constantly underfilled [13, 14]:

$$\mathrm{BTDF} = \frac{L_t}{E_i} = \frac{P_t}{P_i} \cdot \frac{R^2}{A_D \cos\theta_t}. \tag{6}$$

## 2.2. Experiment Setup

We measure absolute values of BTDFs of the different scattering transmissive samples in BxDiff using the NaNoRef setup at PTB, which is originally the national reference setup for measurements of specular reflection [15]. With proper modifications to hardware and the control program, measurements of diffuse transmission could also be performed with modest uncertainty.

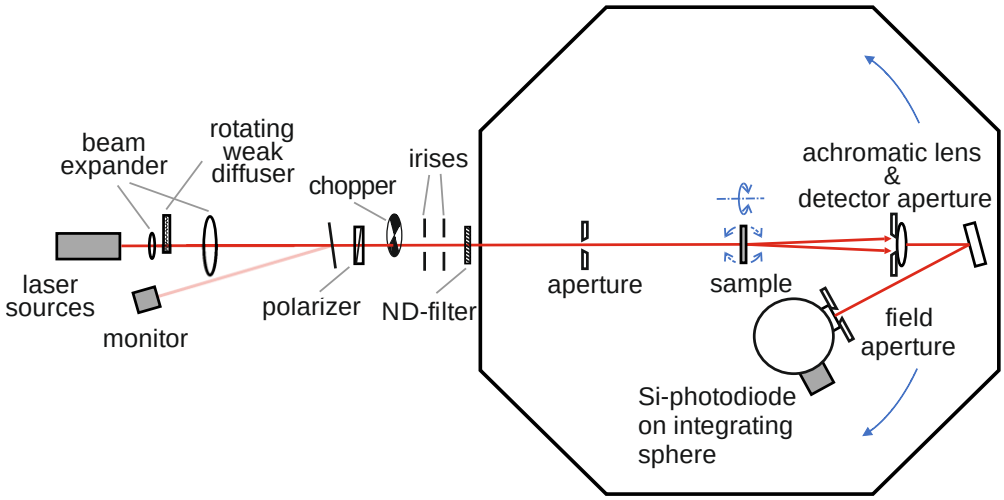


**Figure 2:** Sketch of BTDF setup (modified NaNoRef) at PTB, top view

As illustrated in Figure 2, the central part of the goniometric setup is an octagonal chamber, in which the sample and the detection system are enclosed to eliminate stray light from the light source and ambient light. The sample is placed at the center of this chamber and is irradiated by a collimated beam whose size is restricted by an interchangeable aperture in front of it. The sample holder is a vertical motorized rotary stage which could rotate around its azimuth (optical axis) freely, so that any desired sample azimuth could be achieved. The rotary stage is mounted on a motorized three-axes displacement unit to control the position of the irradiation spot on the sample and to adjust the longitudinal position of the sample back surface on the optical axis. The displacement unit is fixed on a horizontal rotary

table, which rotates around the central (vertical) axis of the octagon. This rotation axis is perpendicular to the optical axis, and the intersection point of these two axes lies exactly on the sample back surface. In this way the polar angle of the incident radiation onto the sample could be controlled. The detection system is mounted on another horizontal rotary arm, which is concentric to the sample rotation table. Therefore, both the table and the arm rotate within the same plane around the same axis, which is referred to as the detection axis.

In the detection system, the detector aperture is interchangeable to different diameters to realize detection with different angular resolutions and detection solid angles. Directly behind the detector aperture, an achromatic lens determines the size of the measurement area $A_M$ (Figure 1(b)) by means of a field aperture, which is placed at the entrance port of an integrating sphere. A calibrated Si-photodiode is mounted on the detection port of it. The use of an integrating sphere homogenizes the radiation for detection and reduces speckle effects as well as polarization-related sensitivity of the detector. All these components of the detection system are fixed on the detection rotary arm and move altogether during detection. The optical path is folded with an angle as small as possible by a planar mirror due to limited space inside the chamber. By alternating the size of the field aperture, the size of the measurement area on the sample back surface could be adjusted. The parameters regarding measurement conditions are listed in Table 1.

**Table 1**
General conditions of BTDF measurement

| Parameter | Notation | Value |
|---|---|---|
| Wavelength | $\lambda$ | 642 nm, 445 nm |
| Azimuth angle of incidence | $\phi_i$ | 0° to 360° |
| Azimuth angle of detection | $\phi_t$ | 0° to 360° |
| Polar angle of incidence | $\theta_i$ | 0° |
| Polar angle of detection | $\theta_t$ | -25° to 80° |
| Irradiation beam size | $A_{\mathrm{beam}}$ | 9.6 / 29.2 / 44.2 / 80.1 mm$^2$ |
| Detector aperture area | $A_D$ | 19.6 / 81.7 / 156.1 mm$^2$ |
| Distance sample to detector | $R$ | 494.5 mm |
| Measurement area on sample (at $\theta_t = 0°$) | $A_M$ | 50.3 / 75.4 / 265.9 mm$^2$ |

Outside of the chamber are the light sources and some beam controlling optics. Two laser sources are used for the measurement, one is a fiber-coupled diode laser at 642 nm and another one is a diode-pumped solid-state laser at 445 nm. To reduce speckle effects, a rotating weak diffuser is placed in the vicinity of the intermediary focus of a beam expander. In this way, the laser beam is expanded to be able to supply varying diameters of the irradiation spot on the sample. Moreover, the coherence of the laser radiation could in this way be reduced and the beam profile is homogeneous after collimation. Polarization of the radiation is controlled by using a half-wave plate and a linear polarizer. Measurements are performed in *s*- and *p*-polarized radiation respectively, with unpolarized detection and then the unpolarized BTDF value was calculated by the mean value out of the two measurement results. The measurement is performed using the lock-in technique to suppress any unwanted optical signals that are not at the chopping frequency. As the BTDF values of different samples vary largely, neutral-density filters are used to bring the detected power to an appropriate level, reducing the influence of electronic noise and improving SNR. The two irises prevent stray light from entering the measurement chamber and filter out the undesired outer parts of the expanded beam. The monitor detector is used to correct for fluctuation in the laser output power.

For an absolute measurement, the sample was firstly moved out of the optical path. The ND-filter was set in and the incident power $P_i$ was measured at $\theta_t = 0°$. Then, the sample was moved into the optical path with its geometric center irradiated. The sample was aligned to have $\theta_i = 0°$ and its azimuth $\phi_i$ (or $\phi_t$ since measurements were all in-plane) was either predefined for rotationally symmetrical samples or predetermined for azimuthally sensitive samples by evaluating the intensity distribution on a screen using a high-resolution camera, which will be introduced in more detail in the next section. A well-defined azimuthal orientation of the sample is of great importance when measured BTDF values

are compared for samples with dedicated azimuthal dependence. The angle-resolved detection of the sample scattering distribution was then carried out by rotating the detector arm to each scatter angle $\theta_t$. The laser beam was not attenuated by the ND-filter when the transmitted scatter signal was measured.

## 2.3. Samples under study

Five types of samples are characterized. Two of them are quasi-Lambertian diffusers with relatively constant BTDF in a large range of scatter angles $\theta_t$. One of them, denoted as HOD-500, is a diffuser made of high purity fused silica (HOD®) manufactured by Heraeus Quarzglas GmbH [16]. It has 50 mm in diameter and 2 mm in thickness and there are micro air bubbles with diameter less than 20 µm uniformly distributed in the bulk volume. Another quasi-Lambertian sample, denoted as Zenith-250, is a 0.25 mm thick foil made of Zenith Polymer®, a high-reflecting material using sintered PTFE powder manufactured by SphereOptics GmbH [17]. It is clamped between two plates with a clear aperture of 45 mm in the center. Types of Mie scattering volume diffuser made of synthetic fused silica, which are similar to HOD-500 [18, 19, 20] and Zenith-250 [20], have been proven to be good near-to-Lambertian diffusers.

The scattering characteristics of the other three types of samples are far away from a Lambertian characteristic. The first one, denoted as DG20-220, is a rotationally symmetrical ground glass diffuser distributed by Thorlabs, Inc [21]. It has 2 inches in diameter and 2 mm in thickness with one side treated using 220 grit polish. Thus, this side of the sample is regarded as the active surface and is irradiated in the measurement. Light is scattered mainly by the surface of this type of sample, leading to a Gaussian-shaped distribution. The second type of sample, denoted as E28-14, is a holographic diffuser provided by Temicon GmbH [22]. It consists of a 125 µm thick imprinted PET foil on standard glass substrate with 2 mm thickness and it has 50 mm edge length. This type of sample has a two-dimensional Gaussian-shaped scattering characteristic, meaning that the FWHM of the scattering distribution is different when varying sample azimuth. The last type among these three, denoted as ED1-S20, is also distributed by Thorlabs, Inc. It is called an Engineered Diffuser™ with 1 inch in diameter and 1.5 mm in thickness. It has a square-shaped scattering distribution and is thus also azimuthally sensitive. The scattering characteristic can be attributed to the individually specified microlens-units on the surface produced by direct laser writing. This type of diffuser is normally used in applications related to beam shaping [23].

For both holographic and engineered diffusers, determination of their azimuthal orientation prior to the measurement must be performed. An air-cooled CCD-camera with 1600 pixels × 1200 pixels resolution was placed towards the back surface of the sample and was horizontally aligned. A half-transparent diffuse screen was placed between the camera and the sample and adjusted to be perpendicular to the beam direction. The sample's scattering distribution falling on the screen could then be photographed by the camera from behind the screen. A series of photos was taken when the azimuth was constantly varied with an interval of 0.1° by the rotary stage holding the sample. The transmitted scattered patterns were then evaluated by different methods and comparable results with an uncertainty of 0.2° regarding the sample azimuthal orientation could be achieved. For the holographic diffuser, its cross section imaged on the screen showed an elliptical form and its $\phi_i = 0°$ orientation was defined when the major axis of the ellipse was parallel to the detection plane. For the engineered diffuser, the $\phi_i = 0°$ orientation was given when one edge of the square-shaped pattern was parallel to the detection plane. The so found orientations were marked by a small dot on the edge of the diffusers for later performed measurements.

# 3. Results

## 3.1. Quasi-Lambertian Diffusers

The measurement results of HOD-500 and Zenith-250 are illustrated in Figure 3(a). Due to the physical limitation on the detection range, results in the negative angle part smaller than -25° are extended by measuring the sample at $\phi_i = 180°$ in the positive angle range greater than 25°, where the

same value ought to be obtained with an ideal measurement setup. This method was also used in the measurement of other samples, when the desired detection range was beyond the limitation.

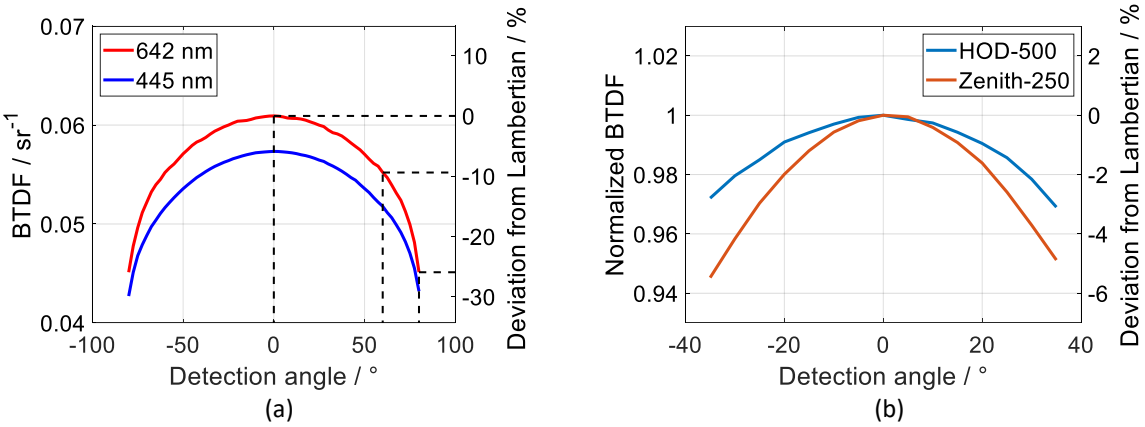


**Figure 3:** (a) BTDF of HOD-500 at 642 nm and 445 nm, $\theta_i = 0°$, $\theta_t$ varies from -80° to 80°; (b) Normalized BTDF of HOD-500 and Zenith-250, $\theta_i = 0°$, $\theta_t$ varies from -35° to 35°

For the sake of brevity only the unpolarized BTDF values of HOD-500 are shown here. Measurement showed similar quasi-Lambertian scattering distributions at both wavelengths, with peak BTDF values of approx. 0.057 $sr^{-1}$ and 0.061 $sr^{-1}$, respectively. The smaller amplitude at 445 nm could be explained by a decrease in the transmittance due to increasing scattering by a larger refractive index at shorter wavelength and a higher absorption as well. The right axis of the plot corresponds to the curve of 642 nm and shows the angle-dependent deviation from a perfect Lambertian diffuser in percentage. At 60° the BTDF drops less than 10% and at 80° approx. 25%, indicating that light is scattered uniformly by HOD-500 within a fairly large range of angles.

The normalized BTDF values of both quasi-Lambertian diffusers are plotted together in Figure 3(b) for an intuitive sample-type comparison. Within a small range of angles from -35° to 35° the discrepancy between the two diffusers already becomes significant. The BTDF of Zenith-250 decreases faster than that of HOD-500 and is thus less "Lambertian". This could be attributed to the different types and sizes of scattering centers in the bulk volume of sample material.

## 3.2. Ground Glass Diffusers and Holographic Diffuser

The measured BTDF values for DG20-220 with fitted curves are shown in Figure 4(a) for 642 nm and 445 nm. Data can be fitted with a Gauss-Lorentz model. Compared to the quasi-Lambertian diffusers this ground glass diffuser has a sharp peak and the distribution is restricted in a small angle area. The FWHM (Full-Width at Half Maximum) are 15.9° at 642 nm and 16.5° at 445 nm. The slightly broader distribution at shorter wavelength might be attributed to enhanced multiple in-surface scattering, which will be discussed in more detail in Section 4.1.

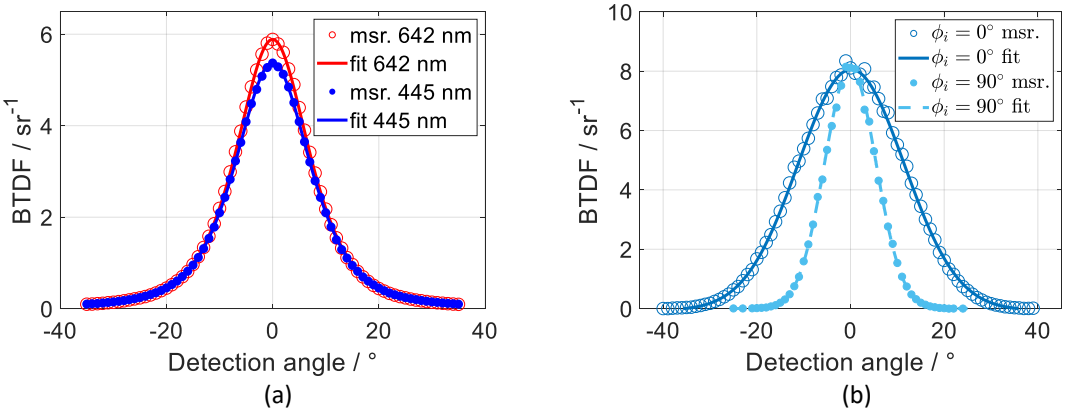


**Figure 4:** BTDF of (a) DG20-220 at 642 nm and 445 nm, $\theta_i = 0°$, $\theta_t$ varies from -35° to 35°; (b) E28-14 at 642 nm, $\phi_i$ at 0° and 90°, $\theta_i = 0°$, $\theta_t$ varies from -40° to 40°

The holographic diffuser E28-14 also has a Gaussian-like scattering characteristic, but the distribution is dependent on its azimuthal orientation. In Figure 4(b), the measured BTDF values with fitted curves at 642 nm at 0° and 90° azimuths are demonstrated. The fit uses the regular Gaussian model. The FWHM values are 26.7° at $\phi_i = 0°$ and 12.9° at $\phi_i = 90°$, indicating that by changing the sample azimuthal orientation of 90° the width of the scatter decreases rapidly to about half of its starting value. Near the peak of the curve at 0° azimuth strong fluctuation in the BTDF values is observed, which might be the effect of laser speckle. The wavelength dependency of E28-14 is similar to that of DG20-220. The peak value is smaller and the FWHMs at both azimuths are slightly larger at 445 nm (not shown).

## 3.3. Engineered Diffusers

BTDF values of the engineered diffuser ED1-S20 at both wavelengths and at both azimuths are illustrated in Figure 5. Its scattering distribution is much different from the other diffusers. From about -7° to 7° the scatter remains almost unchanged, as indicated by the flat top in the curves and then drops rapidly within approx. 3° from peak value to close to zero. Although the scatter pattern is square-shaped, there are still slight differences which could be observed from the angle-resolved measurement at different azimuthal orientations. The wavelength dependency is on one hand similar to that of the surface scattering diffusers. On the other hand, at the two "horns" of the curve the scatter behaves quite distinctively at different wavelengths. This might be attributed to the special microlens structure on the sample surface, whose interaction with light changes with varying wavelength.

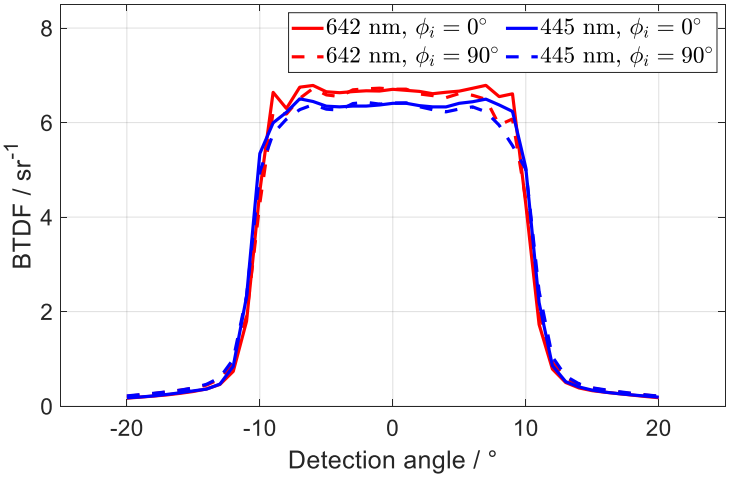


**Figure 5:** BTDF of ED1-S20 at 642 nm and 445 nm, $\phi_i$ at 0° and 90°, $\theta_i = 0°$, $\theta_t$ varies from -20° to 20°

# 4. Discussion

## 4.1. Wavelength Dependency

For a good comparison between different participants within BxDiff, results are to be compared at a certain wavelength. A quasi-standard wavelength is that of the red HeNe-laser: 632.8 nm. For results that are not measured at the prescribed wavelength, a proper correction considering the wavelength-dependent sample properties should be performed. For this purpose, the angle-dependent spectral transmittance of a set of samples was measured on an Agilent Cary 6000i, a commercially available spectrophotometer with Universal Measurement Accessory (UMA) mini-goniometer.

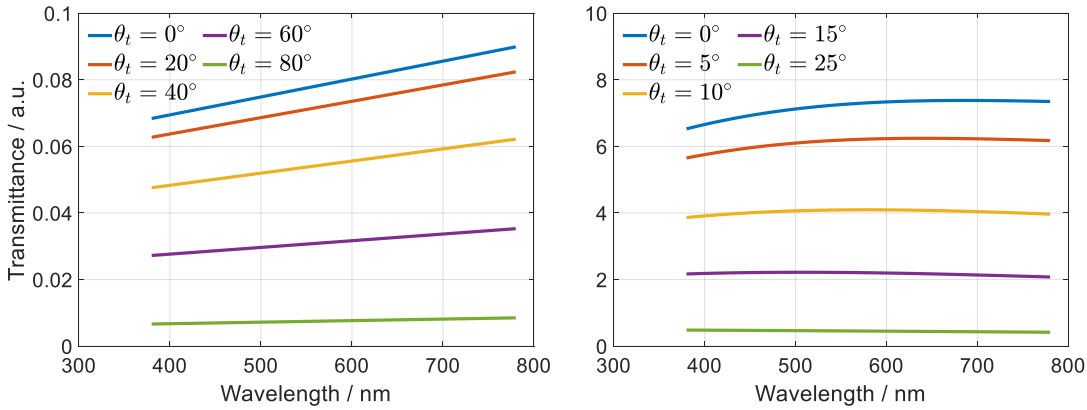


**Figure 6:** Spectral transmittance of (a) Zenith-250 and (b) E28-14 ($\phi_i = 0°$) at different $\theta_t$

In Figure 6(a), the diffuse transmittance into a solid angle of 0.0089 sr of Zenith-250 at different scattering angles is plotted as a function of wavelength. For bulk diffusers, the transmittance is in general fairly proportional to the wavelength. The variation rate or slope of the curve varies with different $\theta_t$. At $\theta_t = 0°$, corresponding to the central peak in the angle-dependent scattering distribution, the BTDF value changes the most with increasing wavelength, whereas at grazing angle $\theta_t = 80°$ the BTDF becomes almost constant and show little spectral dependency. The wavelength dependency is different for surface scattering types. Spectral transmittance of E28-14 is given as an example in Figure 6(b). The spectral transmittance in the central peak of the angular scattering distribution rises with wavelength but flattens at around 600 nm and starts to decrease at even higher wavelengths. The wavelength of the maximum of spectral transmittance $\lambda_{\max}$ also varies with different $\theta_t$. This is observed more clearly by the differential spectral transmittance in Figure 7(a), where the derivatives of transmittance with respect to wavelength are plotted. Interestingly, the wavelength dependency becomes completely "reversed" at larger $\theta_t$. Instead of a positive slope, transmittance decreases constantly with increasing wavelength in the whole VIS. As a result of this wavelength dependency, not only the BTDF value but also the shape of the angle-resolved scattering distribution would be modified by the wavelength correction. For example, correction from a larger wavelength to a smaller one would cause the peak of the distribution to drop while at the falling edges the BTDF would be lifted, resulting in a larger FWHM. This also agrees with the comparison between measured curves of the surface scattering samples at different wavelengths.

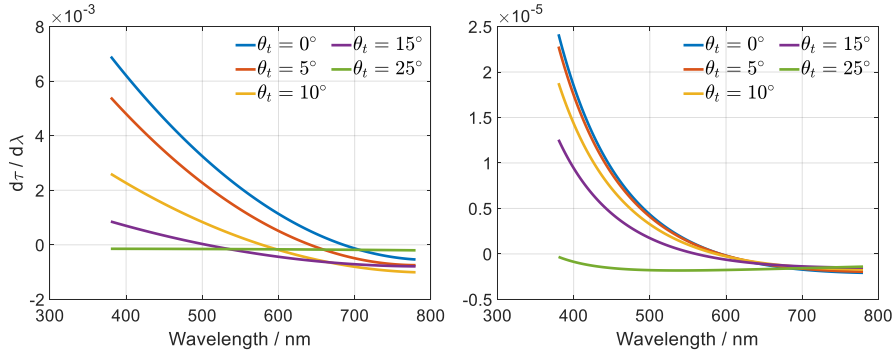


**Figure 7:** Differential spectral transmittance of (a) E28-14 ($\phi_i = 0°$) measured at different $\theta_t$ and (b) simulation using a single scattering model

Scattering effects can likely explain this behavior. We performed a preliminary comparison to simulation results using a single scattering model where a surface scattering sample consists of an active top surface with microfacets and small scattering particles on a smooth transparent substrate. The microfacets obey a normal distribution determined by the surface roughness (standard deviation in height). The calculation is based on Rayleigh scattering where the wavelength dependence is modified

according to particle size by an exponent in [0.0925, 1] (smaller exponent for larger particles). This method has been found to fit reasonably well with the Lorenz-Mie theory [24]. Even without considering multiple scattering, a similar tendency in the simulated spectral transmittance could be observed. This is indicated most clearly by the derivatives of the simulated spectral transmittance demonstrated in Figure 7(b). Compared to the measured one, the magnitude of this simulated effect is smaller, but it is expected to be enhanced by multiple scattering in the sample active surface. Further calculations are in progress and we expect that use of multiple in-surface scattering and scalar diffraction theory can bring the model closer to the observation [25, 26].

## 4.2. Preliminary Uncertainty Analysis

Explicit uncertainty analysis is still in progress. An estimation of the combined measurement uncertainty is around 0.5% ($k = 2$) in the best case ($\theta_t = 0°$) for all sample types. Contributions to the estimated uncertainty budget of HOD-500 at 445 nm and $\theta_t = 0°$, as an example, are listed in Table 2. Determination of the BTDF measurement uncertainty ΔBTDF is performed according to Stover [13]. The uncertainty mainly consists of the statistical errors from the two measured signals, $\Delta P_i$ and $\Delta P_t$, the errors from the measurement of detection solid angle, $\Delta\Omega_t$, and from the receiver's angular position, $\Delta\theta_t$. The combined uncertainty ΔBTDF could be expressed by equation (7):

$$\frac{\Delta\mathrm{BTDF}}{\mathrm{BTDF}} = \sqrt{\left(\frac{\Delta P_i}{P_i}\right)^2 + \left(\frac{\Delta P_t}{P_t}\right)^2 + \left(\frac{\Delta\Omega_t}{\Omega_t}\right)^2 + \left(\frac{\Delta\theta_t \cdot \sin\theta_t}{\cos^2\theta_t}\right)^2}. \tag{7}$$

At other angles the measurement uncertainty varies mainly with the measured signal amplitude and the cosine value of the detection angle. For both quasi-Lambertian samples, ΔBTDF remains unchanged in a large angle area and eventually increases to over 2% at grazing angles. For the other three types of samples, the signal amplitude drops quickly at the edges of the scattering distribution, leading to a sharp increase in the total uncertainty, from 0.5% to more than 3%. This estimate might hold only for slowly varying BTDF characteristics. At least for parts of the scattering distributions depicting a sudden variation, a term proportional to $\frac{\Delta\mathrm{BTDF}}{\Delta\theta_t}$ must be added to the final uncertainty budget.

**Table 2**
Preliminary uncertainty budget of HOD-500, at $\lambda = 445$ nm, $\theta_t = 0°$

| Source | Notation | Relative uncertainty |
|---|---|---|
| Irradiation power | $\Delta P_i$ | 0.00031 |
| Scattered transmitted power | $\Delta P_t$ | 0.00014 |
| Detection solid angle | $\Delta\Omega_t$ | 0.00153 |
| Distance sample to detector | $\Delta R$ | 0.00054 |
| Detector aperture area | $\Delta A_D$ | 0.00134 |
| ND-filter | $\Delta\tau_F$ | 0.00268 |
| Receiver angle | $\Delta\theta_t$ | 0.00005 |
| Estimated total uncertainty ($k = 2$) | ΔBTDF | 0.005 / 0.5% |

## 5. Conclusion

Preliminary results of the BTDF measurement involved in the EMPIR project BxDiff are presented in this paper. Five types of transmissive diffusers, two bulk scattering, one pure surface scattering, one holographic and one with engineered surface, were measured at the modified NaNoRef setup of PTB with a preliminary total uncertainty of approx. 0.5% ($k = 2$) at 0° detection angle (corresponds to the angle of specular transmission). The angle-dependent spectral transmittance of all samples was measured using a commercially available spectrophotometer to provide supporting information for a possible wavelength-dependent correction for the benefit of the comparison at a prescribed wavelength. An interesting phenomenon of the interaction between angle- and wavelength-dependency of the spectral transmittance was observed for the holographic diffuser and possible explanations are proposed

from first-step simulation results. Further study on the wavelength dependence of different sample types will be carried out to provide a more detailed quantitative explanation. Our aim is to acquire thorough information on the relation between sample microscopic structures and their scattering properties as well as a better knowledge of BTDF measurement on optical translucent materials with high precision.

## 6. Acknowledgements and Disclaimer

The authors gratefully thanks Eva Velke for the calibration of ND-filters used in the measurement and Marius Bagusch for providing measurement data of the area of different apertures used in the measurement. We also thank the members of the mechanical workshop Morten John, Jörn Hauffe, Marcel Janik and Henry Ganz for the construction of several mechanical parts of the setup.

We gratefully acknowledge the support of the Braunschweig International Graduate School of Metrology B-IGSM.

The results reported in this paper are derived from activities within the frame of the EMPIR project 18SIB03 BxDiff (New quantities for the measurement of appearance), that has received funding from the EMPIR programme co-financed by the Participating States and from the European Union's Horizon 2020 research and innovation programme.

The mentioned diffusers dealt with in this paper are examples of commercially available products only and using these specific diffusers in investigations does not constitute an endorsement of these products by the authors or their institutions.

## 7. References

[1] E. Hilsenrath, D. Williams, J. Frederick, Calibration of Long Term Data Sets from Operational Satellites Using the Space Shuttle, in: Proceedings of SPIE 0924, Recent Advances in Sensors, Radiometry, and Data Processing for Remote Sensing, SPIE Press, Orlando, United States, 1988, pp. 215-222. doi:10.1117/12.945689.

[2] M. R. Dobber, R. J. Dirksen, G. H. J. van den Oord, R. H. M. Voors, Q. Kleipool, G. Jaross, M. Kowalewski, E. Hilsenrath, G. W. Leppelmeier, J. de Vries, W. Dierssen, N. C. Rozemeijer, Ozone monitoring instrument calibration, IEEE Transactions on Geoscience and Remote Sensing 44 (2006) 1209-1238. doi:10.1109/TGRS.2006.869987.

[3] R. Pawluczyk, Holographic diffusers, in: Proceedings of SPIE 2042, Photopolymers and Applications in Holography, Optical Data Storage, Optical Sensors, and Interconnects, SPIE Press, Quebec City, Canada, 1994, pp. 156-169. doi:10.1117/12.166350.

[4] R. Bräuer, F. Wyrowski, O. Bryngdahl, Diffusers in digital holography, Journal of the Optical Society of America A 8 (1991) 572-578. doi:10.1364/JOSAA.8.000572.

[5] G. Baranoski, J. Rokne, An Algorithmic Reflectance and Transmittance Model for Plant Tissue, Computer Graphics Forum 16 (1997) C141-C150. doi:10.1111/1467-8659.00150.

[6] J. Gu, R. Ramamoorthi, P. N. Belhumeur, S. K. Nayar, Dirty Glass: Rendering Contamination on Transparent Surfaces, in: 18th Eurographics Symposium on Rendering, The Eurographics Association, Grenoble, France, 2007, pp. 159–170. doi:10.2312/EGWR/EGSR07/159-170.

[7] Q. Dai, J. Wang, Y. Liu, J. Snyder, E. Wu, B. Guo, The Dual-microfacet Model for Capturing Thin Transparent Slabs, Computer Graphics Forum 28 (2009) 1917-1925. doi:10.1111/j.1467-8659.2009.01570.x.

[8] M. Papas, K. de Mesa, H. Jensen, A Physically-Based BSDF for Modeling the Appearance of Paper, Computer Graphics Forum 33 (2014) 133-142. doi:10.1111/cgf.12420.

[9] EMPIR project 18SIB03 BxDiff Homepage, 2022. URL: https://bxdiff.cmi.cz/.

[10] F. E. Nicodemus, Directional Reflectance and Emissivity of an Opaque Surface, Applied Optics 4 (1965) 767-775. doi:10.1364/AO.4.000767.

[11] F. E. Nicodemus, J. C. Richmond, J. J. Hsia, I. W. Ginsberg, T. Limperis, Geometrical Considerations and Nomenclature for Reflectance, National Bureau of Standards, Washington, D.C., 1977.

[12] F. O. Bartell, E. L. Dereniak, W. L. Wolfe, The Theory and Measurement of Bidirectional Reflectance Distribution Function (BRDF) and Bidirectional Transmittance Distribution Function

(BTDF), in: Proceedings of SPIE 0257, Radiation Scattering in Optical Systems, SPIE Press, Huntsville, United States, 1980, pp. 154-160. doi:10.1117/12.959611.
[13] J. Stover, Optical scattering, 3rd. ed., SPIE Press (Society of photo-optical instrumentation engineers), Bellingham, Washington, United States, 2012.
[14] J. J. Butler, G. T. Georgiev, C. C. Cooksey, Comparison of bidirectional transmittance distribution function (BTDF) measurements on fused silica and sintered polytetrafluoroethylene diffusers, Metrologia 56 (2019) 065008. doi:10.1088/1681-7575/ab4523.
[15] A. Schirmacher, S. Hesse, E. Velke, The new reference set-up for regular spectral transmittance and reflectance at PTB, in: Proceedings of NEWRAD 2014, Espoo, Finland, 2014, pp. 221-222. URL: http://newrad2014.aalto.fi/Newrad2014_Proceedings.pdf
[16] Heraeus Group, 2022. URL: https://www.heraeus.com/en/group/home/home.html.
[17] SphereOptics, 2022. URL: https://sphereoptics.de/.
[18] D. F. Heath, G. Georgiev, Characteristics of a new type of Mie scattering volume diffuser and its use as a spectral albedo calibration standard for the solar reflective wavelength region, in: Proceedings of SPIE 8153, Earth Observing Systems XVI, SPIE Press, San Diego, California, United States, 2011, pp. 321-334. doi:10.1117/12.892109.
[19] P. Lemaillet, H. J. Patrick, T. A. Germer, L. Hanssen, B. C. Johnson, G. T. Georgiev, Goniometric and hemispherical reflectance and transmittance measurements of fused silica diffusers, in: Proceedings of SPIE 9961, Reflection, Scattering, and Diffraction from Surfaces V, SPIE Press, San Diego, California, United States, 2016, pp. 996109. doi:10.1117/12.2237975.
[20] G. T. Georgiev, J. J. Butler, K. Thome, C. Cooksey, L. Ding, Preliminary results of BTDF calibration of transmissive solar diffusers for remote sensing, in: Proceedings of SPIE 9972, Earth Observing Systems XXI, SPIE Press, San Diego, California, United States, 2016, pp. 997205. doi:10.1117/12.2235802.
[21] Unmounted N-BK7 Ground Glass Diffusers, Thorlabs Inc., 2022. URL: https://www.thorlabs.com/newgrouppage9.cfm?objectgroup_id=1132&pn=DG20-220.
[22] Mikrostrukturen und Nanostrukturen | temicon GmbH, 2022. URL: https://www.temicon.de.
[23] Engineered Diffusers™, Thorlabs, Inc., 2022. URL: https://www.thorlabs.com/newgrouppage9.cfm?objectgroup_id=1660&pn=ED1-S20.
[24] J. R. Mourant, T. Fuselier, J. Boyer, T. M. Johnson, I. J. Bigio, Predictions and measurements of scattering and absorption over broad wavelength ranges in tissue phantoms, Applied Optics 36 (1997) 949-957. doi:10.1364/ao.36.000949.
[25] J. R. Frisvad, S. A. Jensen, J. S. Madsen, A. Correia, L. Yang, S. K. S. Gregersen, Y. Meuret, P.-E. Hansen, Survey of Models for Acquiring the Optical Properties of Translucent Materials, Computer Graphics Forum 39 (2020) 729–755. doi:10.1111/cgf.14023.
[26] V. Falster, A. Jarabo, J. R. Frisvad, Computing the Bidirectional Scattering of a Microstructure Using Scalar Diffraction Theory and Path Tracing, Computer Graphics Forum 39 (2020) 231-242. doi:10.1111/cgf.14140.